Nanoscale

Semiconductor-to-conductor transition in 2D copper (II) oxide nanosheets through surface sulfur-functionalization

Journal:	*Nanoscale*
Manuscript ID	NR-ART-03-2020-002208.R1
Article Type:	Paper
Date Submitted by the Author:	23-Jun-2020
Complete List of Authors:	Montgomery, Matthew; Yale University, Department of Chemical & Environmental Engineering Sugak, Nikita; Yale University, Department of Chemical & Environmental Engineering Yang, Ke; Yale University, Department of Chemistry Rogers, James; Yale University, Department of Chemical & Environmental Engineering Kube, Sebastian; Yale University, Department of Mechanical Engineering & Materials Science Ratinov, Anthony; Yale University, Department of Chemical & Environmental Engineering Schroers , Jan; Yale University, Department of Mechanical Engineering & Materials Science Batista, Victor; Yale University, Department of Chemistry Pfefferle, Lisa; Yale University, Department of Chemical & Environmental Engineering

Semiconductor-to-conductor transition in 2D copper (II) oxide nanosheets through surface sulfur-functionalization

Matthew J. Montgomery[a]*, Nikita Sugak[a]*, Ke R. Yang[b], James M. Rogers[a], Sebastian A. Kube[c], Anthony C. Ratinov[a], Jan Schroers[c], Victor S. Batista[b], Lisa D. Pfefferle[a]

[a] Department of Chemical and Environmental Engineering, Yale University, PO Box 208286, New Haven CT USA

[b] Department of Chemistry, Yale University PO Box 208286, New Haven CT 06520-8286 USA

[c] Department of Mechanical and Materials Science Engineering, Yale University PO Box 208286, New Haven CT 06520-8286 USA

*These authors contributed equally to this work

Corresponding Author: Matthew Montgomery

PO Box 208286, New Haven CT 06520-8286 USA

Abstract

Functionalization is a widely-used strategy to modulate and optimize the properties of materials towards various applications, including sensing, catalysis, and energy generation. While the influence of sulfur-functionalization of carbon materials and oxides like ZnO and TiO_2 has been studied, far less research has been devoted to analyzing sulfur-functionalization of CuO and other transition metal oxide nanomaterials. Here, we report sulfur-functionalization of copper (II) oxide nanosheets synthesized by using a soft-templating procedure, with sulfur-addition based on hydrogen sulfide gas as a source. The resulting sulfur-functionalization does not change the overall crystal structure and morphology of the CuO nanosheets, but leads to a decrease in surface hydroxyl groups. Sulfur induces a semiconductor-to-conductor state transition of the CuO nanosheets, which is supported by computational modeling. The metallic transition results from shifting of the Fermi level into the valence band due to formation of Cu-S bonds on the surface of the CuO nanosheets.

Key Words

Sulfur functionalization, 2D transition metal oxide, copper oxide nanosheets, hydrogen sulfide, density-functional theory

1) Introduction

Functionalization and doping are synthetic strategies frequently used in synthesis to modulate the properties of materials [1]. Functionalization often involves the use of foreign elements or molecules to change the nature of bonding at the surface, or within the bulk of the material. Doping is a specific type of functionalization intended to modulate electronic, or optical properties of semiconductors with foreign elements that replace native lattice atoms, or fill interstitial sites. The new elements, usually in very small amounts (much less than 1% by mole fraction), introduce electronic states that change the overall electronic properties [2-4] Functionalization, however, is a more general process with the added impurities often in excess of 1%.

The interplay between different material properties can be critical for specific applications. For instance, the catalytic activity of metal catalysts supported on metal oxides has been correlated with specific metal-support interactions [5] as well as to the band gap [6]. In materials for charge transfer applications, correlations between electronic properties have been found. For example, previous studies suggest that the conductivity in n-type ZnO thin films correlates predominantly to the optical band gap, and precursor molarity [7]. Ali et al. have shown that the band gap of tin-doped indium oxide films increases as the annealing temperature is increased, which occurs with a concomitant reduction in the resistivity of the material [8].

Sulfur is a chemically versatile element that has been widely used in functionalization chemistry. Many experimental studies have focused on functionalizing carbon nitride [9, 10], carbonaceous systems [11-15], and oxides such as TiO_2 [16-18] with sulfur for enhanced catalytic and photocatalytic reactivity [9, 16, 19], energy storage [20], and other applications. For instance, sulfur-functionalized graphene is found to significantly improve the high specific capacity of

lithium-ion batteries when utilized as anode materials [13]. Sulfur-doped hematite shows high stability, as well as improved photoelectrochemical activity after doping [21]. Inhomogeneous sulfur-doping has also been shown to improve the conductivity in C_{60} films at room temperature due to ionization of electrons in the impurity bands, making doped grains metallic in nature [14]. First principle calculations on tin selenide provide evidence that sulfur-doping increases the Seebeck coefficient while lowering thermal and electrical conductivity [22].

Computational studies additionally highlight the potential for sulfur to be applied in the tuning of material optical properties. For example, An et al. have used first-principle studies to show that substitution of lattice oxygen with sulfur in α-$Fe_2O_{3-0.17}S_{0.17}$ reduces the band gap to 1.45 eV, which approaches an optimal band gap for solar cell applications as suggested by the Shockley-Queisser limit [23]. Umebayashi et al. showed that experimentally synthesized sulfur-doped TiO_2 exhibits a narrower band gap compared with its undoped counterpart. *Ab-initio* calculations suggest this is due to a mixing of the S3p states with the valence band [17]. Experimental and theoretical studies on the effect of sulfur-functionalization in graphene, g-C_3N_4, ZnO, and even diamond can be found in the literature [9-13, 15, 20, 24], demonstrating the various ways in which sulfur can be used to modulate band structure and improve catalytic properties. Despite these reports, there is a lack of both experimental and theoretical studies on sulfur-functionalization in a number of other materials, particularly transition metal oxides like CuO, MnO_2, NiO, and CoO. Experimental observations and theoretical calculations need to be validated against one another in order to accurately determine structure-property and property-property relationships which will guide the development of advanced materials for next-generation applications.

To begin providing an experimental and computational understanding of the effect of sulfur-functionalization on the properties of understudied nanomaterials, we focus on transition metal oxides, namely the copper (II) oxide (CuO) system. CuO is a p-type semiconductor that has been the subject of growing interest in many fields, including photocatalysis [25], batteries [26], supercapacitors [27], and sensors [28]. The indirect band gap for CuO has been reported to range from ~1 eV to 1.4 eV [29, 30]. Literature values for the direct transitions in CuO range widely, however, varying anywhere from 1.6 to 3.2 eV, in part attributed to the differences in the Cu-O stoichiometry [30, 31]. Compared to its bulk counterpart, CuO nanosheets exhibit a higher reactivity and are more amenable for property engineering because of the larger ratio of exposed surface atoms. In previous work, the band gap of CuO nanosheets was shown to be influenced by the stoichiometry of copper to oxygen, and was able to be tuned using oxidative heat treatments [31]. Few studies, however, have looked at the effect of sulfur on the properties of CuO nanomaterials. Navaee et al. reported on the superior photo-electrocatalytic activity of sulfur-doped Cu_2O/CuO nanoclusters. In the sample mixture, which contained 0.25% sulfur by atomic ratio, sulfur-doping slightly increased the optical band gap from 1.95 eV to 2.05 eV [32]. Other reports on sulfur-doping in metal oxides report a general trend of narrowing the band gap [17, 23]. Aside from these studies, there are also reports on sulfur-doped Cu/Co oxides and CuS-doped CuO nanoparticles [33, 34].

In this study, the influence of sulfur-functionalization on the properties of CuO nanosheets was analyzed. In order to minimize interference from elements other than sulfur on material properties, hydrogen sulfide gas (H_2S) was used as the sulfur-source for the functionalization experiments. Previous studies concerning the reaction of H_2S with Cu and Cu-O surfaces focus on the corrosion properties of bulk materials [35-38] or H_2S-sensing applications [39, 40], but less

work has been done to study the effect of H_2S-treatment as a means for tuning the properties of nanomaterials. CuO nanosheets functionalized with sulfur were prepared under various treatment times, and their properties were characterized using Fourier Transform-Infrared (FT-IR) spectroscopy, X-ray diffraction (XRD), scanning electron microscopy (SEM), X-ray photoelectron spectroscopy (XPS), and diffuse-reflectance spectroscopy (DRS). The resistivities of CuO nanosheets before and after functionalization with sulfur were also characterized as a function of temperature. The experiments were supplemented with density functional theory (DFT) calculations to provide a theoretical understanding of how sulfur modulates CuO properties.

2) Methods

2.1 Sulfur-Functionalization Procedure Using Hydrogen Sulfide

CuO nanosheets with thicknesses between 15 to 30 nm were synthesized through a soft-templating method described previously [31], but with modifications to ensure the optical band gap of the starting CuO material falls within a 0.1 eV-range. Because the band gap can be related to other material properties, such as catalytic activity or conductivity, experiments analyzing the effect of doping/functionalization on material properties should be done on a material with consistent starting properties, batch-to-batch. In our previous work [31] it was found that the copper-to-oxygen stoichiometry of CuO nanosheets significantly influences the optical band gap. The synthesis reported in [31], which employs a large reaction volume and yields ~1 g of CuO nanosheets, results in CuO with band gaps that may vary anywhere from 1.5 to 2.0 eV batch-to-batch. That is, the measured optical gap of CuO nanosheets from one synthesis is repeatable across multiple trials, but the optical gaps of CuO nanosheets between different batches could vary considerably. This observation is attributed to non-uniformities in the reaction environment due

to the large reaction volume, which can lead to inconsistent copper-to-oxygen ratios in the product obtained batch-to-batch. To mitigate these issues, we utilize a small volume, Ar-blanketed technique for synthesizing CuO nanosheets, described in greater detail in the electronic supplementary information (ESI) section 1, in order to ensure a consistent optical band gap batch-to-batch (ESI Fig. 1 and 2, ESI Table 1).

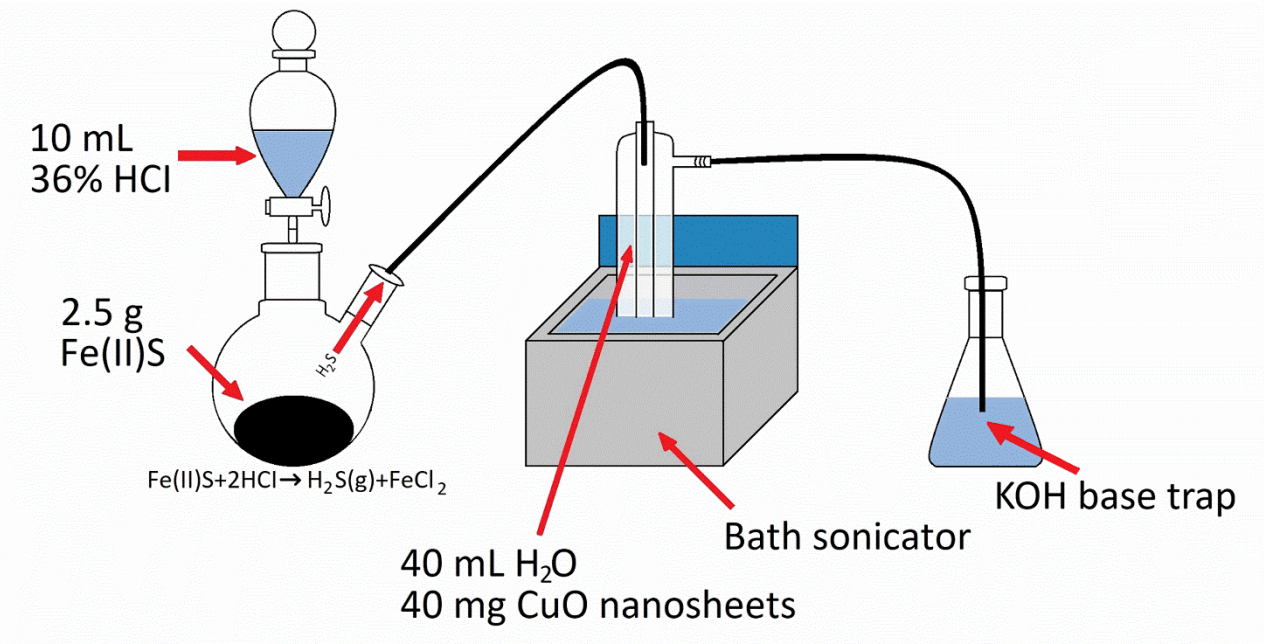

Figure 1- Depiction of experimental setup used for sulfur-functionalization experiments.

The experimental setup for sulfur-functionalization of the CuO nanosheets is shown in Figure 1. For the procedure, 40 mg of CuO nanosheets were added to 40 mL of DI water, placed in a vacuum trap, and subsequently placed in a gentle bath sonicator (Cole-Parmer Model No. 08849-00). Then, 2.5 g of iron sulfide (99%, Sigma-Aldrich) was added to a two-neck round-bottom flask (volume = 500 mL) and connected to the vacuum trap. A funnel containing 10 mL 36% HCl (J.T. Baker) was attached to the round-bottom flask. The entire volume of HCl was added to the iron sulfide and sealed, which generated H_2S gas. At this point, the sulfur-functionalization reaction was considered to have started. The H_2S bubbled through the solution containing the dispersed CuO nanosheets, providing the sulfur-source. The KOH base trap serves to create a back-pressure

and limits the amount of H_2S able to escape the reactor. All experiments were performed at room temperature with varying treatment times, up to 15 minutes. The temperature of the dispersed mixture changed by no more than 10°C over the course of the reaction. After the reaction, the samples were filtered. The precipitate was washed with DI water in excess. After filtration, the samples were vacuum dried at room temperature, ground, and placed under vacuum in a desiccator before further measurements.

2.2 X-Ray Diffraction

XRD patterns were collected on a Rigaku SmartLab X-ray diffractometer using a Cu Kα source with a beam energy of 8.04 eV (λ = 1.5406Å). Powder samples were measured on glass slides and data analysis was performed using PDXL-2 Rigaku software.

2.3 Scanning Electron Microscopy

Images of the CuO nanosheets were collected on a Hitachi SU-70 scanning electron microscope. The acceleration voltage was set to 5 or 10 kV. Samples were prepared for SEM by pressing the powders onto double-sided carbon tape. Multiple spots were examined to confirm the sample was uniform.

2.4 Fourier-Transform Infrared Spectroscopy

The FT-IR spectra of the powder samples were collected with a Thermo Nicolet 6700 FT-IR Spectrometer. The reported data were collected in the range of 500 to 4000 cm^{-1}, and averaged over 32 scans. The background signal was collected over 8 scans before every sample was analyzed.

2.5 X-Ray Photoelectron Spectroscopy

The XPS spectra were collected using a monochromatic 1486.7 eV Al Kα X-ray source on a PHI VersaProbe II X-ray Photoelectron Spectrometer with a 0.47 eV system resolution. The energy scale has been calibrated using Cu $2p_{3/2}$ (932.67 eV) and Au $4f_{7/2}$ (84.00 eV) peaks on a clean copper

plate and a clean gold foil, respectively. Powder samples were pressed onto double-sided scotch tape on the sample holder. For region scan, regular power (200u50W15kV), 23.500 eV Pass Energy and 0.1000 eV step size were used, and each spectrum was swept multiple times to improve accuracy. Data analysis was performed with a software package in CasaXPS. Atomic concentrations were calculated according to the following equation

$$AC_{\mathrm{x}}(\%) = \frac{A_{\mathrm{x}}/\mathrm{R.S.F}}{A_1/\mathrm{R.S.F} \ldots + A_{\mathrm{n}}/\mathrm{R.S.F}} \qquad (1)$$

where AC stands for atomic concentration, R.S.F is relative structural factor (obtained from the manufacturer), n is the total number of different categorized atoms, and x is the index for the element of interest.

2.6 Band Gap Measurements

The optical band gaps of our samples were measured using diffuse reflectance spectroscopy (DRS). A Shimadzu 2600 UV-Vis spectrometer with an integrating sphere attachment was used for this purpose. This technique is beneficial because it allows us to analyze the optical properties of unsupported nanomaterial powders, and utilizes the enhanced scattering intrinsic to powder samples. By using DRS as opposed to UV-Vis absorption spectroscopy, light scattering effects in the absorption spectra due to the media the powders are suspended in can be avoided [41]. In this technique, powder samples are pressed into the center of the sample holder, and light from 1100 nm to 300 nm is directed towards the sample. The samples were pumped under vacuum in a desiccator overnight and were removed from the desiccator directly before measurements. Barium sulfate powder was used as the reference sample for all measurements. The diffusely scattered light from the powder samples was collected by the integrating sphere and focused on to the detector. The reflectance spectrum was then transformed via a Kubelka-Munk (KM)

transformation to a plot in which direct and indirect optical band gaps could be extracted. This technique has been validated by measuring the band gaps of bulk zinc oxide (ESI section 2, ESI Fig. 3 and 4, ESI Table 2), and was used to measure the band gaps of the materials in this work.

2.7 Electrical Transport Measurements

Approximately 20 mg of material was pressed into pellets (diameter = 5 mm) under an applied load of two tons for 20 seconds using a Carver No. 3851-0 Model C 12-ton press. For resistivity measurements, thin films serving as electronic contacts were fabricated using confocal DC magnetron co-sputtering (AJA International ATC 2200). The pellets were secured to a substrate holder and covered by masks made of cellulose acetate transparency film in order to selectively cover the pellet surface for contact fabrication. The sputtering sources were pointed at the rotating samples at an angle of 29.8^{0} towards the normal axis in order to produce films of homogeneous thickness. The processing chamber was evacuated to a base pressure level of less than 5.0E-7 Torr, then the films were sputtered in flowing ultra-high purity argon at a pressure of 5.8E-3 Torr. First, a 200 nm-thick adhesion layer of nickel was deposited at a sputtering power of 150 W, then 600 nm of gold was deposited at a sputtering power of 100 W. The target purities were 99.99% for both the nickel and the gold target. The resulting contacts (length x width= 0.5 mm x 0.5 mm), were co-linear, with a center-to-center spacing of approximately 1.2 mm.

To prepare the samples for four-probe electrical transport measurements, the pellets were secured to a Dynacool resistivity sample puck using carbon tape, and aluminum wires were bonded from the puck to the contacts on the pellets using a West Bond 747630E-79 wire bonder. Transport measurements were then taken using a Quantum Design PPMS DynaCool using the ETO option. The AC resistance was measured as a function of temperature from 250 K to 100 K. Resistance values were then converted to resistivities based on the following equation [42]:

$$\rho\ (\Omega\ \mathrm{cm}) = \frac{\pi}{\ln 2} * t\ (\mathrm{cm}) * R\ (\Omega) \qquad (2)$$

where t is the thickness of the pellet samples and R is the measured resistance of the sample. Excitation frequencies at 18 or 21 Hz were analyzed, as the imaginary contribution to the measured resistance was negligible at these frequencies. This equation is used to correct for the thickness and contact spacing, since the pellet thickness (~0.5 mm - 0.7 mm) is on the order of half the center-to-center spacing of the contacts on the pellets (~0.6 mm).

2.8 DFT Calculations

We used the Vienna ab initio simulation package (VASP) [43-46] version 5.4.1 for all periodic boundary calculations. The projector augmented plane wave (PAW) method [47, 48] together with the Perdew-Burke-Ernzerhof (PBE) exchange-correlation functional [49] were employed to describe the electron-ion interactions. We used the PBE + U method following Dudarev's approach [50] to add on-site potentials to the *d* electrons of transition metals to describe the electronic states of transition metal oxides properly. In addition, a U_{eff} = U - J parameter of 7.5 eV was used for CuO to reproduce the experimental band gaps of bulk metal oxides. A cutoff of 450 eV was chosen for the plane wave basis set in all calculations. A 7 × 7 × 7 Monckhorst-Pack type k-point grid [51] was chosen for the optimization of bulk CuO. A Gaussian smear was used and the σ value was chosen to be 0.1 eV. The energy convergence criterion was set to be 10^{-5} eV per unit cell and the force convergence criterion of 0.03 eV $Å^{-1}$ was used for all structure optimizations. A supercell with dimensions of 4.69 Å × 3.43 Å × 25.26 Å and OH termination was used to model the CuO (002) surface, which is able to reproduce the experimentally-observed band gap of the CuO nanosheets. A 3 × 3 × 1 Monkhorst-Pack k-point mesh was used for all slab optimization calculations. All atoms were allowed to relax during the geometry optimization. For density of states (DOS) calculations, we used a 7 × 7 × 1 Monkhorst-Pack k-point mesh and the Gaussian

Smear Method with a σ value of 0.1 eV to obtain accurate electronic DOS. The symmetric points Γ, X, M, Y are used to generate the K-path in the band structure calculations according to previous studies for 2D materials [52]. The visualization of structures and figure preparation were done with VESTA software package version 3 [53].

3) Results and Discussion

The aim of this study was to elucidate the influence of sulfur-functionalization on the properties of 2D transition metal oxide nanomaterials, which was achieved by reacting CuO nanosheets with H_2S for varying time intervals. To test if the H_2S reaction converted the CuO nanosheets to another phase, introduced functional groups to the surface of the nanosheets, or destroyed the two-dimensional nature of the material, XRD, FT-IR, and SEM were performed on pure and H_2S-treated CuO nanosheets. As can be seen in Figure 2, the XRD patterns remain largely unchanged after the sulfur-treatment for all reaction conditions. All of the samples adopt the tenorite crystal structure [54]. No other phases were detected in the CuO nanosheets before or after the sulfur-treatment, although the intensities of the peaks between 35-40° noticeably increase as the treatment time increases. An increase in the intensities of the peaks from 45 to 80° was also observed after the sulfur-treatment. The increase in peak intensities after sulfur-functionalization is mainly attributed to the higher X-ray scattering factor for sulfur relative to oxygen.

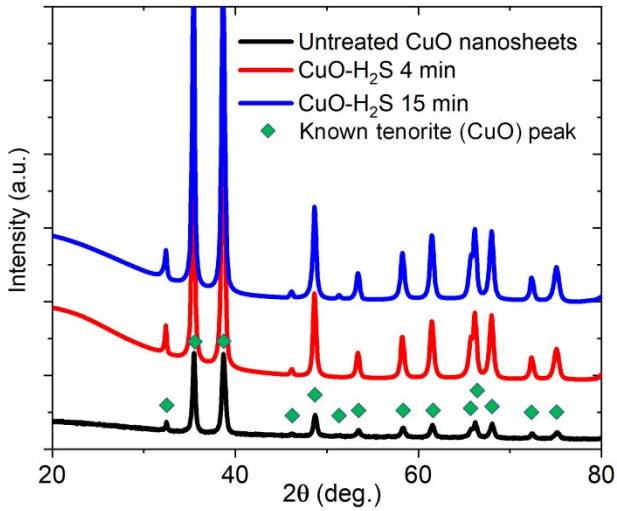

Figure 2- XRD Patterns of untreated and H_2S-treated CuO nanosheets. The known tenorite (CuO) peaks come from reference [54].

The morphologies of the different CuO samples were examined using SEM, as shown in Figure 3. All of the samples display a 2D nanosheet structure. However, relative to the pure CuO nanosheets, the H_2S-treated nanosheets have slightly rounder edges. This could be attributed to the mild sonication used during the sulfur-functionalization reaction, which may introduce defects at the edges of the CuO nanosheets. From these analyses, it can be concluded that the H_2S-functionalization procedure does not significantly alter the crystal structure or morphology of the CuO nanosheets, thus maintaining the crystalline, 2D nature of the samples.

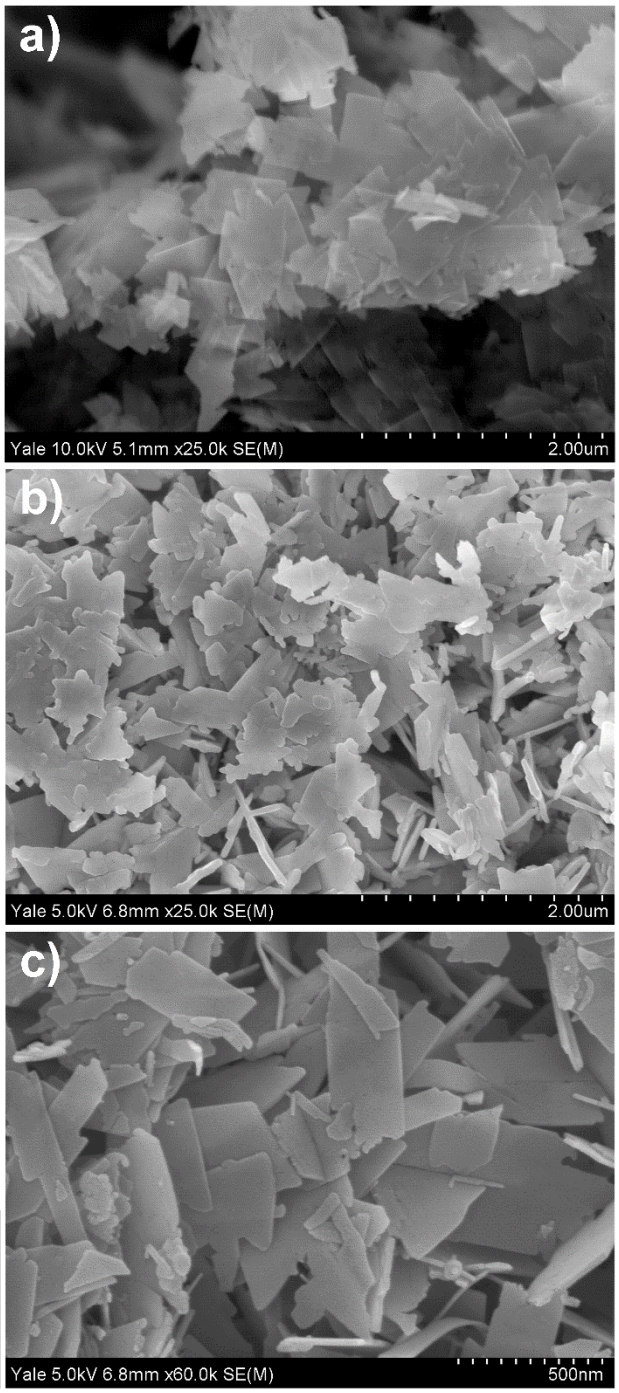

Figure 3- SEM micrographs of untreated and H_2S-treated CuO samples a) Untreated CuO sample b) 4-minute treated sample c) 15-minute treated sample

The samples were also examined using FT-IR spectroscopy, with the results shown in Figure 4. Data from 1900 to 2250 cm^{-1} were excluded due to an instrument artefact. Peaks are observed near 480 and 600 cm^{-1}, known to correspond to Cu-O vibrations [55]. A broad peak between 3200 to 3600 cm^{-1} is also observed in the pure CuO nanosheets, attributed to surface hydroxyl

groups [56, 57]. This peak persists in the 4-minute sample, but becomes noticeably smaller for the 15-minute sample. This implies that at larger treatment times, the H_2S-treatment removes surface hydroxyls. A small peak is also visible in the pure CuO nanosheets near 1600 cm^{-1}, which is attributed to O-H bending modes. The peak near 1350 cm^{-1} in the pure CuO nanosheets is attributed to CO_2 adsorbed to the surface of the nanosheets, which has been observed in the FT-IR spectra of other CuO nanostructures [58-60]. The H_2S treatment appears to remove these peaks, however, as this peak is not present in the spectra for any of the H_2S-treated samples. These results show that the H_2S treatment does not introduce any new functional groups to the material in significant quantities to be detected, and rather decreases the presence of OH and other moieties.

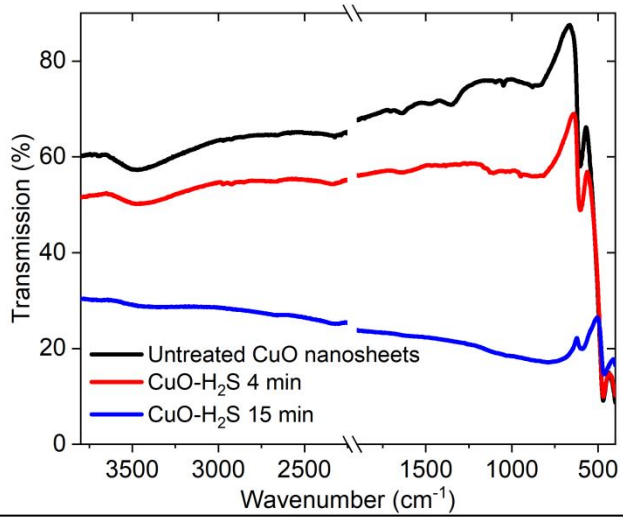

Figure 4 – FT-IR spectra of pure and H_2S-treated CuO nanosheets

XPS, a surface-sensitive technique with an information depth of ~ 1-10 nm, was performed on all of the samples to analyze the surface structure and sulfur content of the samples. Only copper, oxygen, carbon, and, for the H_2S-treated samples, sulfur were detected (ESI section 3, ESI Fig. 7; ESI section 4, ESI Tables 4-6). The relative percentages of surface copper, oxygen, and sulfur are shown in Table 1. For the pure CuO, the relative percentage of surface oxygen begins at 51%, with the oxygen content decreasing with increasing H_2S-treatment time. Concomitant with an increase in the H_2S-treatment time is a steady increase in the relative percentage of surface sulfur, ranging from 2% up to 13%. Surprisingly, the relative amount of surface copper increases slightly from the untreated to 4-minute H_2S-treated sample, from 51% to 53% for the 4-minute sample. These results suggest that, from the untreated to 4-minute sample, sulfur and copper replace surface oxygen. From the 4-minute to 15-minute sample, however, a decrease in the surface copper content was observed, concomitant with an increase in the surface sulfur content. It should be noted that copper and oxygen are roughly in the stoichiometric ratio for the 15-minute sample (43% Cu vs. 44% O). If sulfur was being incorporated into the CuO lattice by preferentially replacing oxygen or copper, one would expect the relative copper-to-oxygen ratio to diverge from unity. This could mean that sulfur replaces both copper and oxygen in the CuO lattice during longer treatment times of 15 minutes. However, if sulfur replaces copper ions in the CuO lattice,

Table 1- Relative percentages of copper, oxygen, and sulfur in untreated and H_2S-treated CuO nanosheets. These values were calculated based on regional scan data of the $Cu2p_{3/2}$, O1s, and S2p regions shown in ESI Tables 4-6, assuming the carbon content is all due to surface contamination. Error in percentages is approximately ± 1% point.

	Copper	**Oxygen**	**Sulfur**
Untreated CuO	51%	49%	0%
H_2S-CuO 4 minutes	53%	45%	2%
H_2S-CuO 15 minutes	43%	44%	13%

one would also expect to see evidence of sulfur in a positive oxidation state. While the S2p region of the 15-minute sample contains a broad peak from 168-170 eV corresponding to oxidized sulfate species, this peak is small and it is clear that reduced sulfur species dominate the surface of this material (Fig. 5c). This suggests that it is unlikely that sulfur replaces copper during the functionalization procedure. Additionally, the increase in sulfur could be explained by the formation of sulfur layers on the CuO surface. This scenario could explain the increase in surface sulfur content while keeping relative ratios of copper to oxygen near unity, and is supported by computational simulations discussed further on.

All of the samples exhibited similar XPS spectra in the Cu2p region (Fig. 5), displaying characteristic $Cu2p_{1/2}$ peaks at 953.4, as well as Cu^{2+} satellite peaks from 940-945 and 962.6 eV. The samples all show a peak in the $Cu2p_{3/2}$ region at ~933.5 eV, attributed to Cu-O bonds from the CuO. However, for a treatment time of 15 minutes, an additional peak centered at ~932.5 eV appears, suggesting that copper is present in a reduced state relative to the Cu^{2+} in the CuO. This is likely due to the formation of Cu-S bonds, as CuS and Cu_2S are known to have $Cu2p_{3/2}$ peaks centered between 932.2-932.5 eV [61]. In the S2p region, the untreated sample exhibits no sulfur, as expected, but peaks are present in the spectra for all of the H_2S-treated samples. At all treatment times, one peak was observed at 162.2 eV, attributed to thiols/Cu-S species. At longer treatment times, a low-intensity, broad peak at 169 eV appears, corresponding to oxidized sulfur species. All samples exhibited one main peak at 529.7 eV in their O1s spectra, corresponding to lattice oxygen. A shoulder at 531.8 eV, attributed to surface hydroxyls and adsorbed water, is present in the untreated CuO nanosheets. This shoulder grows more apparent and shifts to slightly higher binding energies with increasing treatment time. In past studies on CuO nanosheets, functionalization processes were found to shift the peaks corresponding to lattice oxygen and

surface hydroxyls to slightly higher binding energies [62]. Note also that a small, broad peak centered near 168 eV was observed in the S2p region of the 15-minute sample, corresponding to the formation of S-O bonds from species such as sulfates. Therefore, the shift in the O1s peaks to slightly higher binding energies is attributed primarily to changes in the environment of oxygen from the restructuring of the nanosheet surface during the functionalization procedure, and secondarily from the formation of a small amount of surface sulfate species. One peak was observed in the C1s region for all of the samples, attributed to adventitious carbon contamination at 284.8 eV.

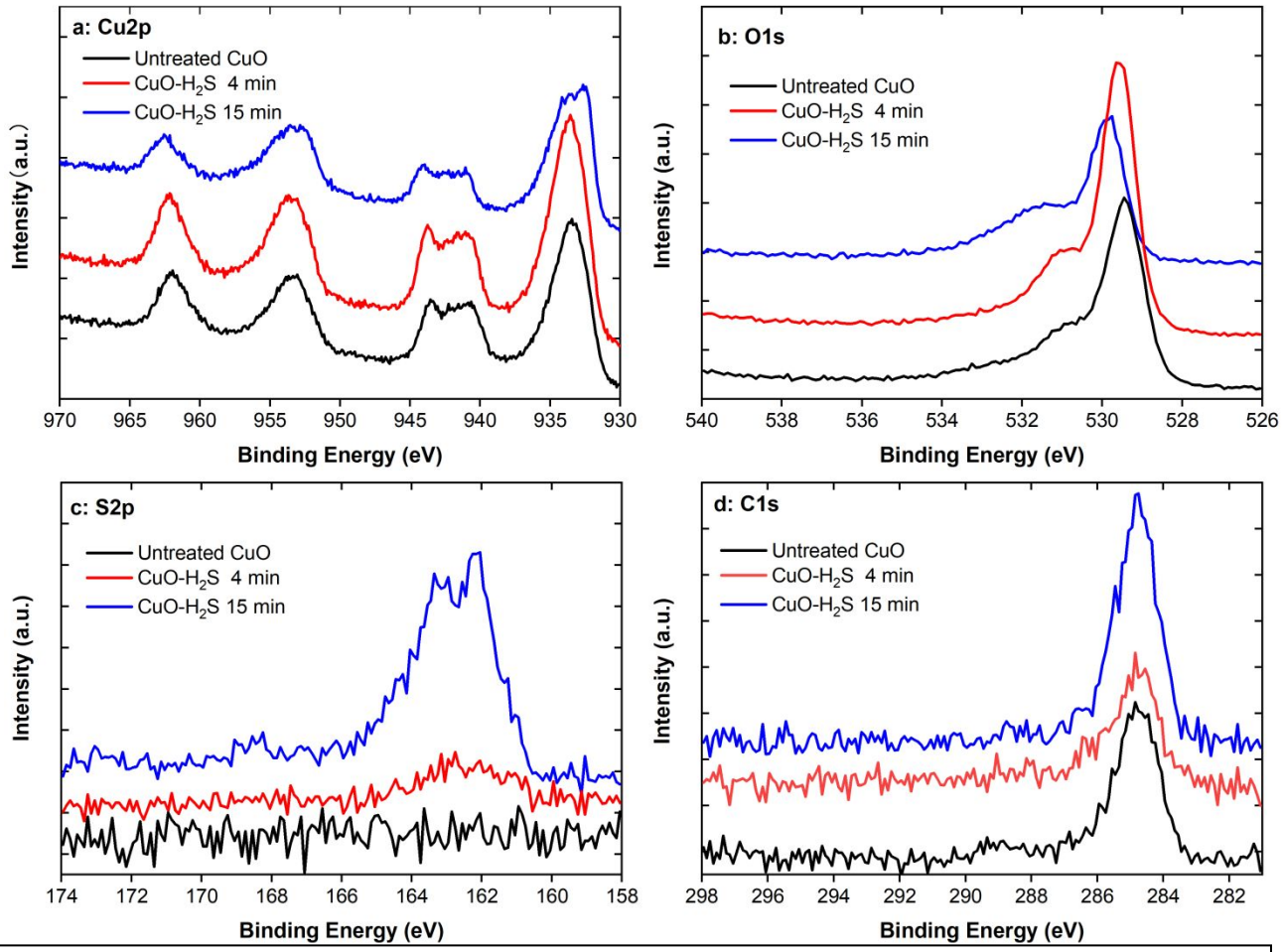

Figure 5- XPS region spectra for untreated and H_2S-treated CuO nanosheets. a) Copper 2p region b) Oxygen 1S region c) Sulfur 2p region d) Carbon 1s region

The reflectance spectra of the samples were measured and transformed to plots from which direct and indirect optical gap energies could be calculated (ESI Fig. 5 and 6). It is known that, for wavelengths near the energy gap value, the absorption coefficient has a square dependence for direct transitions, and square root dependence for indirect transitions [63]. For the range of photon energies analyzed, one direct optical transition and one indirect optical transition were observed. The values for these gaps are shown in ESI Table 3. The indirect and direct optical transitions observed in the pure CuO nanosheets (1.33 and 1.71 eV, respectively) are in agreement with literature values [29-31]. With increasing time of H_2S-treatment (and subsequently increasing sulfur content), a slight decrease in the indirect and direct gaps is observed. Although small, there is a significant difference in the optical gaps between the 15-minute sample and all of the other samples. This slight decrease in optical band gap with sulfur-functionalization mirrors similar results obtained by calculations on sulfur-doping in a wide variety of systems, including metal oxides [17, 23]. Previous studies on sulfur-doped Cu-O nanostructures noted a slight increase in the optical gap with sulfur-doping [32]. However, the sulfur-doping procedure in [32] was performed on a mixed Cu_2O/CuO material, and it is not clear at this time if the observed increase in band gap can be attributed to sulfur-incorporation into CuO, Cu_2O, or a coupled composite of the two materials.

The resistivities of pure CuO nanosheets and 15-minute H_2S-treated CuO nanosheets were measured as a function of temperature using a four-point probe technique, and are shown in Figure 6. Because of the granular nature of the powder samples, disk-shaped pellets were prepared for electrical transport measurements. The pure CuO nanosheets displayed a resistivity value near 900 Ω*cm at 250 K, with resistivity increasing by over two orders of magnitude as the sample cooled from 250 K to 150 K. This behavior in electrical transport with decreasing temperature is

indicative of a semiconducting/insulating material, and is expected since pure CuO is a semiconductor. As temperature decreases, thermal energy also decreases, which makes it more difficult to promote electrons from the valence band to the conduction band in CuO.

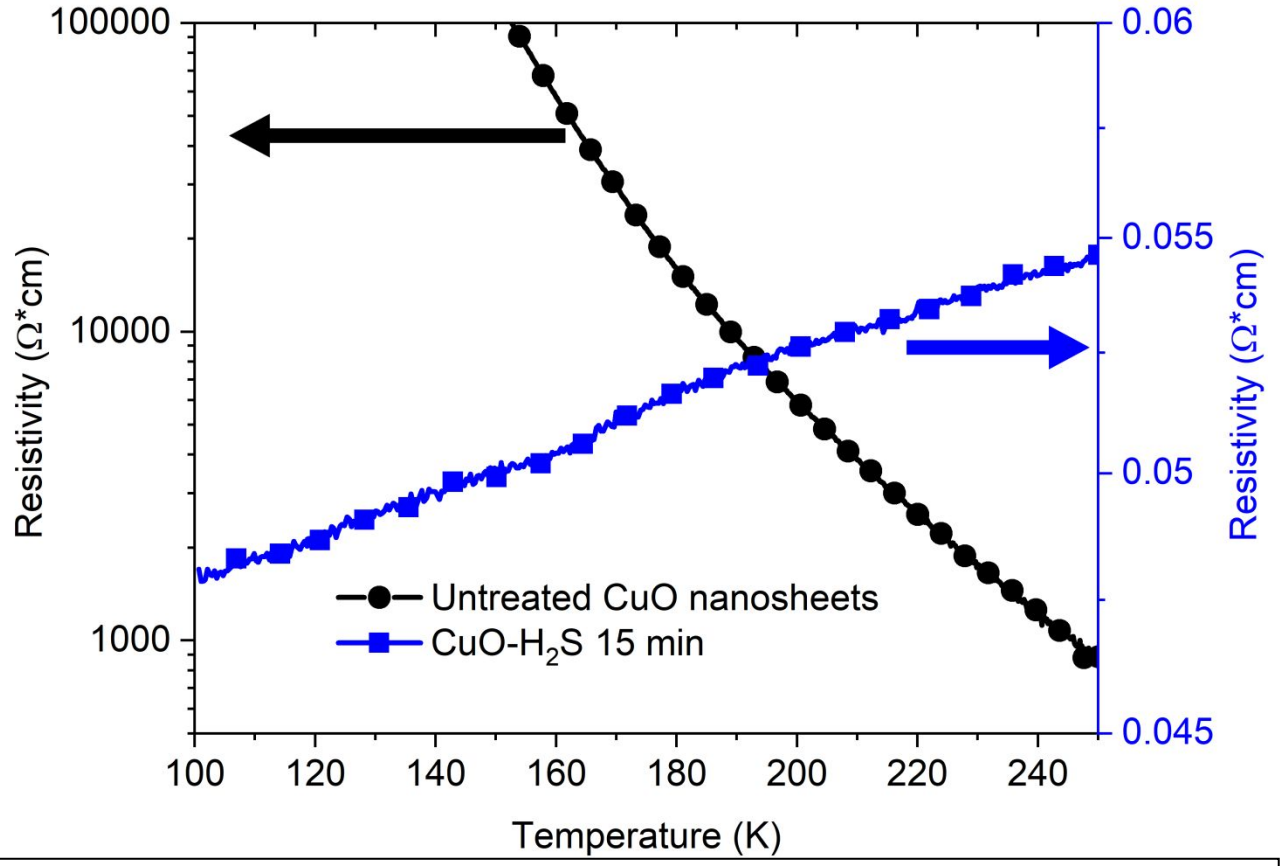

Figure 6- Resistivity of pellets made from pure CuO nanosheets (●, black, left axis) and 15-minute H_2S-treated CuO nanosheets (■, blue, right axis). Every 20th datapoint is denoted with a marker.

The resistivity of the 15-minute H_2S-CuO sample, however, was found to be over three orders of magnitude lower than that of the pure CuO nanosheets across all examined temperatures. In addition, the resistivity of the sample decreases from 250 K to 100 K, demonstrating behavior indicative of a metallic conductor. For metals, as temperature decreases, atomic lattice vibrations also decrease. Since states already populate the conduction band of metals, decreasing temperature lessens the effect of electron scattering by the lattice, leading the resistivity to also decrease with temperature. This is a somewhat counter-intuitive result, as the XRD pattern for

this sample suggests that it is composed only of copper oxide (tenorite). Therefore, one may expect the transport properties to be similar to that of CuO, which generally have large resistivities on the order of 10^2-10^5 Ohms*cm [64-66] because of their semiconducting/insulating nature. The only difference between the two samples is the degree of sulfur-functionalization, and perhaps slight changes in nanostructure (Fig. 3) which may weakly affect transport properties. No other phases are present in the 15-minute H_2S-treated CuO sample (Fig. 2), implying that the metallic behavior must be attributed to the sulfur-functionalization process of the CuO nanosheets. This mirrors similar results obtained in copper oxide-based sensors, in which conductance increases when the oxide is exposed to H_2S, permitting the amperometric detection of H_2S. The explanation for this observation includes the formation of a percolating network of Cu-S clusters on the surface of the oxide, the formation of a conductive Cu-O-S surface layer, or S^{2-}-diffusion into the bulk of the material [39, 40]. Our results suggest the formation of a sulfur/Cu-S layer on the surface of the CuO nanosheets, and the DFT calculations, discussed further on, confirm that the hypothesized surface structure is feasible and accurately reflects the material properties. It should be noted that the room temperature resistivity of a pellet from the 4-minute H_2S-treated CuO sample was tested and found to be comparable to that of the pure CuO nanosheets, implying that a larger level of sulfur than is in the 4 minute sample is needed in order to induce metal-like behavior.

To explore the transition to metal-like behavior upon sulfur-functionalization, DFT calculations were performed with a slab model of the CuO (002) surface as in our previous study [62]. We considered the sulfur-functionalization effect by replacing a ½ layer and monolayer of surface OH groups to SH groups, consistent with experimental FT-IR data which suggest a decrease in hydroxyl groups with increasing H_2S-treatment time. DFT-optimized structures are shown in Figure 7. The structure of the ½ layer-SH CuO (002) surface are very similar to the

untreated CuO (002) structure, but S atoms sit above the O atoms due to their larger size. Significant surface structure reconstruction is observed when a monolayer of SH groups replaces the surface OH groups. In fact, half of surface Cu atoms are pulled out by SH groups. We checked the spin density at Cu centers and found the 3-coordinated surface Cu^{2+} get reduced to Cu^{+}, consistent with the Cu^{+} peak observed in the XPS results.

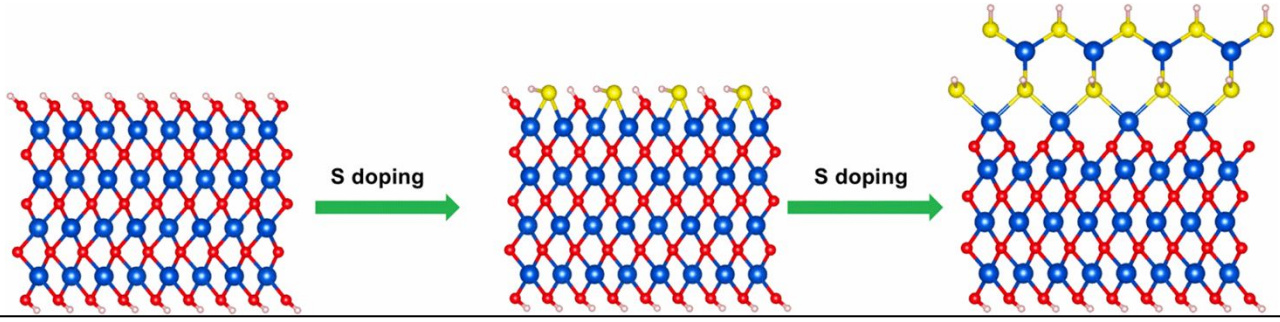

Figure 7- DFT optimized structures of untreated CuO (002) surface, CuO (002) surface with ½ monolayer SH, and CuO (002) surface with 1 monolayer SH. Blue, red, yellow, and white balls represent Cu, O, S, and H atoms, respectively

We computed the DOS of the untreated and sulfur-functionalized CuO (002) slab models and the results are shown in Figure 8. The corresponding band structures are displayed in ESI Fig. 8-10. The calculated band gap of the CuO (002) slab is ~ 1.7 eV, indicating it is a p-type semiconductor with the Fermi level sitting slightly above the valence band. This value of the electronic band gap is also in agreement with the direct gap determined from optical analyses (ESI Table 3). For the ½ layer SH on the CuO (002) surface, replacement of OH groups with SH groups causes the position of the conduction band minimum to decrease slightly (Fig. 8b), leading the overall electronic band gap to decrease. When a monolayer of SH groups is formed on the CuO (002) surface, however, the electronic band gap becomes 0 (Fig. 8c). This is because the Fermi level is shifted into the valence band, where electronic states are now populated. Figure 8c reveals that the states available at the Fermi energy due to sulfur-functionalization are primarily

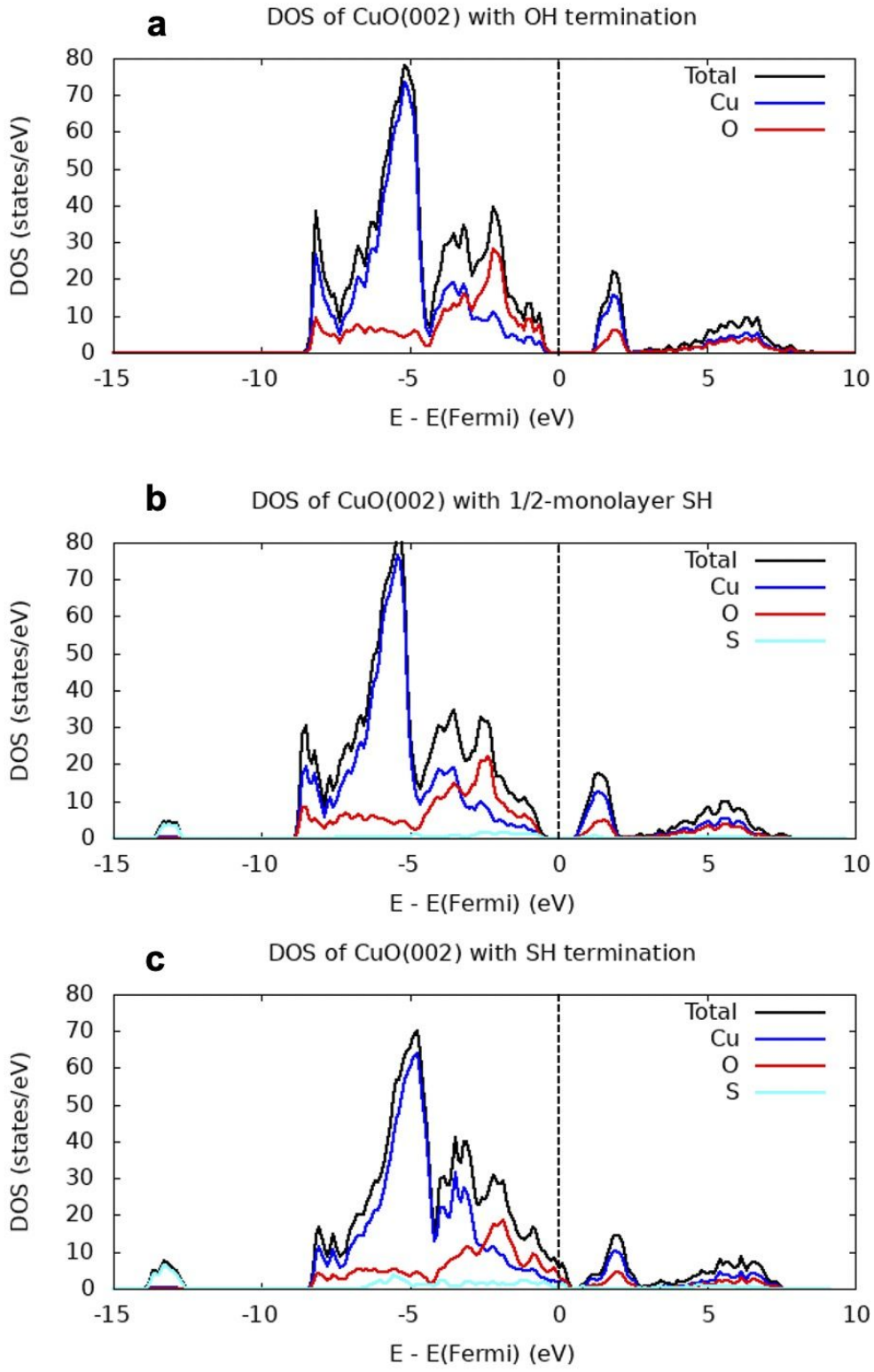

Figure 8. Calculated total and projected density of states (DOS) of (a) untreated CuO (002) surface, (b) CuO (002) surface with ½-monolayer of SH groups, and (c) CuO (002) surface with one monolayer of SH groups. The vertical dashed line shows the Fermi energy.

attributed to oxygen atoms. As shown in Figure 7, when the surface OH groups are replaced by a full layer of SH groups, the surface Cu^{2+} and S^{2-} atoms undergo restructuring, forming a $(Cu\text{-}S)_3$ six-membered ring structure. Some of the surface Cu^{2+} atoms are further reduced to Cu^{+}, as indicated by our simulations. These large geometry distortions raise the energy level of the interfacial oxygen atoms, providing states closer to the Fermi energy and inducing metallic behavior in the functionalized nanosheets. The metallic transition predicted by the simulations is consistent with the experimental resistivity measurements, which show conductive behavior upon sulfur-functionalization. Furthermore, the observation that the Fermi energy is pushed to the valence band with functionalization implies that the surface Cu-S structures are behaving analogously to a p-type dopant, thereby increasing the concentration of holes rather than electrons.

It should be noted that the electronic band gap obtained from the DOS calculations is different than the optical gaps determined via DRS. Our band structure calculations (ESI section 5, ESI Fig. 8-10) show that the CuO (002) nanosheet is an indirect semiconductor. By functionalizing the CuO nanosheet with sulfur, the band gap decreases until it becomes a metal with electronic states populated near the Fermi energy. Near the **Γ** point, however, there are several bands that are well-separated and may be responsible for our observed optical band gaps. It is possible for materials which behave as metals, such as degenerate semiconductors, to produce non-zero apparent band gaps when probed with optical techniques [67, 68]. Thus, it is possible for a material to have an electronic band gap of zero while possessing a non-zero optical band gap.

4) Conclusions

We have determined the effect of sulfur-functionalization via H_2S gas on the properties of CuO nanosheets. The functionalization procedure did not significantly alter the CuO nanosheet crystal structure or the morphological properties, although the optical band gaps decreased slightly. We found that the functionalization procedure introduced Cu-S bonds on the nanosheet surface by removing surface hydroxyl groups, inducing a semiconductor-to-conductor transition. The DFT simulations reveal that the formation of Cu-S bonds on the CuO surface introduces holes as the main impurity and consequently shifts the Fermi level into the valence band, leading to the observed metallic behavior upon sulfur-functionalization.

5) Conflicts of Interest

The authors declare no conflicts of interest.

6) Acknowledgements

This material is based upon work supported by the Army Research Office. This work is also supported by the National Energy Research Scientific Computing Center and Air Force Office of Research. The XPS, XRD, and PPMS measurements were performed at the Yale West Campus Materials Characterization Core. The SEM images were taken at the Yale Institute for Nanoscience and Quantum Engineering. The FT-IR experiments were performed at the Yale Chemical and Biophysical Instrumentation Center. Additionally, the authors would like to acknowledge Dr. Min Li for his helpful conversations related to X-ray characterization techniques. VSB acknowledges an allocation of high-performance computer time from the National Energy Research Scientific Computing Center (NERSC) and support by the Air Force Office of Scientific Research (AFOSR) grant #FA9550-13-1-0020.

7) References

1. Schubert, E.F., *Doping in III-V semiconductors*. 2015: E. Fred Schubert.
2. Uchida, S., et al., *Optical spectra of La 2− x Sr x CuO 4: Effect of carrier doping on the electronic structure of the CuO 2 plane.* Physical Review B, 1991. **43**(10): p. 7942.
3. Stolbov, S. and S. Zuluaga, *Sulfur doping effects on the electronic and geometric structures of graphitic carbon nitride photocatalyst: insights from first principles.* Journal of Physics: Condensed Matter, 2013. **25**(8): p. 085507.
4. Zhou, X., J. Shi, and C. Li, *Effect of metal doping on electronic structure and visible light absorption of SrTiO3 and NaTaO3 (Metal= Mn, Fe, and Co).* The Journal of Physical Chemistry C, 2011. **115**(16): p. 8305-8311.
5. Lai, X. and D.W. Goodman, *Structure–reactivity correlations for oxide-supported metal catalysts: new perspectives from STM.* Journal of Molecular Catalysis A: Chemical, 2000. **162**(1-2): p. 33-50.
6. Getsoian, A.B., Z. Zhai, and A.T. Bell, *Band-gap energy as a descriptor of catalytic activity for propene oxidation over mixed metal oxide catalysts.* Journal of the American Chemical Society, 2014. **136**(39): p. 13684-13697.
7. Benramache, S., et al., *Correlation between electrical conductivity—optical band gap energy and precursor molarities ultrasonic spray deposition of ZnO thin films.* Journal of Semiconductors, 2013. **34**(11): p. 113001.
8. Ali, D., et al., *Correlation between structural and optoelectronic properties of tin doped indium oxide thin films.* Optik, 2017. **128**: p. 235-246.
9. Hong, J., et al., *Mesoporous carbon nitride with in situ sulfur doping for enhanced photocatalytic hydrogen evolution from water under visible light.* Journal of Materials Chemistry, 2012. **22**(30): p. 15006-15012.
10. Lin, S., et al., *Mechanistic insight into the water photooxidation on pure and sulfur-doped g-C3N4 photocatalysts from DFT calculations with dispersion corrections.* Journal of Molecular Catalysis A: Chemical, 2015. **406**: p. 137-144.
11. Bhattacharjya, D., et al., *Graphene nanoplatelets with selectively functionalized edges as electrode material for electrochemical energy storage.* Langmuir, 2015. **31**(20): p. 5676-5683.
12. Yang, Z., et al., *Sulfur-doped graphene as an efficient metal-free cathode catalyst for oxygen reduction.* ACS nano, 2012. **6**(1): p. 205-211.
13. Yun, Y.S., et al., *Effects of sulfur doping on graphene-based nanosheets for use as anode materials in lithium-ion batteries.* Journal of Power Sources, 2014. **262**: p. 79-85.
14. Gong, J., et al., *Enhancement of electrical conductivity in sulfur-doped C60 films.* Thin solid films, 1997. **302**(1-2): p. 256-259.
15. Zhou, H., et al., *Quantum chemical calculations of sulfur doping reactions in diamond CVD.* Japanese Journal of Applied Physics, 2001. **40**(4S): p. 2830.
16. Yang, C., et al., *Core-shell nanostructured "black" rutile titania as excellent catalyst for hydrogen production enhanced by sulfur doping.* Journal of the American Chemical Society, 2013. **135**(47): p. 17831-17838.
17. Umebayashi, T., et al., *Band gap narrowing of titanium dioxide by sulfur doping.* Applied Physics Letters, 2002. **81**(3): p. 454-456.
18. Tian, F. and C. Liu, *DFT description on electronic structure and optical absorption properties of anionic S-doped anatase TiO2.* The Journal of Physical Chemistry B, 2006. **110**(36): p. 17866-17871.
19. Lin, Y., et al., *Enhanced visible light photocatalytic activity of Zn2SnO4 via sulfur anion-doping.* Materials Letters, 2009. **63**(13-14): p. 1169-1171.
20. Ma, Z., et al., *Sulfur-Doped Graphene Derived from Cycled Lithium–Sulfur Batteries as a Metal-Free Electrocatalyst for the Oxygen Reduction Reaction.* Angewandte Chemie International Edition, 2015. **54**(6): p. 1888-1892.

21. Bemana, H. and S. Rashid-Nadimi, *Effect of sulfur doping on photoelectrochemical performance of hematite.* Electrochimica Acta, 2017. **229**: p. 396-403.
22. Jayaraman, A., M. Molli, and V. Kamisetti. *Effect of sulfur doping on thermoelectric properties of tin selenide–A first principles study*. in *AIP Conference Proceedings*. 2015. AIP Publishing LLC.
23. Xia, C., et al., *Tuning the band gap of hematite α-Fe2O3 by sulfur doping.* Physics Letters A, 2013. **377**(31-33): p. 1943-1947.
24. Cho, J., et al., *Sulfur-doped zinc oxide (ZnO) Nanostars: Synthesis and simulation of growth mechanism.* Nano Research, 2012. **5**(1): p. 20-26.
25. Yao, M.-h., et al., *Photocatalytic activity of CuO towards HER in catalyst from oxalic acid solution under simulated sunlight irradiation.* Transactions of Nonferrous Metals Society of China, 2010. **20**(10): p. 1944-1949.
26. Wang, B., et al., *Synthesis of CuO/graphene nanocomposite as a high-performance anode material for lithium-ion batteries.* Journal of Materials Chemistry, 2010. **20**(47): p. 10661-10664.
27. Dubal, D.P., et al., *Mild chemical strategy to grow micro-roses and micro-woolen like arranged CuO nanosheets for high performance supercapacitors.* Journal of Power Sources, 2013. **242**: p. 687-698.
28. Choi, J.D. and G.M. Choi, *Electrical and CO gas sensing properties of layered ZnO–CuO sensor.* Sensors and actuators B: Chemical, 2000. **69**(1-2): p. 120-126.
29. Marabelli, F., G. Parravicini, and F. Salghetti-Drioli, *Optical gap of CuO.* Physical Review B, 1995. **52**(3): p. 1433.
30. Al-Gaashani, R., et al., *Synthesis and optical properties of CuO nanostructures obtained via a novel thermal decomposition method.* Journal of Alloys and Compounds, 2011. **509**(35): p. 8761-8769.
31. Fishman, Z.S., et al., *Fundamental role of oxygen stoichiometry in controlling the band gap and reactivity of cupric oxide nanosheets.* Journal of the American Chemical Society, 2016. **138**(34): p. 10978-10985.
32. Navaee, A. and A. Salimi, *Sulfur doped-copper oxide nanoclusters synthesized through a facile electroplating process assisted by thiourea for selective photoelectrocatalytic reduction of CO2.* Journal of colloid and interface science, 2017. **505**: p. 241-252.
33. Chen, C., et al., *Sulfur-doped copper-cobalt bimetallic oxides with abundant Cu (I): A novel peroxymonosulfate activator for chloramphenicol degradation.* Chemical Engineering Journal, 2019. **361**: p. 1304-1316.
34. Fu, T., *CuS-doped CuO nanoparticles sensor for detection of H2S and NH3 at room temperature.* Electrochimica Acta, 2013. **112**: p. 230-235.
35. Tran, T., C. Fiaud, and E. Sutter, *Oxide and sulphide layers on copper exposed to H2S containing moist air.* Corrosion Science, 2005. **47**(7): p. 1724-1737.
36. Sharma, S., *Reaction of copper and copper oxide with H 2 S.* Journal of The Electrochemical Society, 1980. **127**(1): p. 21-26.
37. Sansregret, J., *Reaction of Copper Oxide with H 2 S.* Journal of The Electrochemical Society, 1980. **127**(9): p. 2083-2084.
38. Galtayries, A. and J.P. Bonnelle, *XPS and ISS studies on the interaction of H2S with polycrystalline Cu, Cu2O and CuO surfaces.* Surface and interface analysis, 1995. **23**(3): p. 171-179.
39. Hennemann, J., et al., *Copper oxide based H2S dosimeters–Modeling of percolation and diffusion processes.* Sensors and Actuators B: Chemical, 2015. **217**: p. 41-50.
40. Sauerwald, T., et al. *H2S detection utilizing percolation effects in copper oxide*. in *Proceedings Sensor*. 2013.
41. Morales, A.E., E.S. Mora, and U. Pal, *Use of diffuse reflectance spectroscopy for optical characterization of un-supported nanostructures.* Revista mexicana de física, 2007. **53**(5): p. 18-22.
42. Miccoli, I., et al., *The 100th anniversary of the four-point probe technique: the role of probe geometries in isotropic and anisotropic systems.* Journal of Physics: Condensed Matter, 2015. **27**(22): p. 223201.
43. Kresse, G. and J. Hafner, *Ab initio molecular dynamics for liquid metals.* Physical Review B, 1993. **47**(1): p. 558.

44. Kresse, G. and J. Hafner, *Ab initio molecular-dynamics simulation of the liquid-metal–amorphous-semiconductor transition in germanium.* Physical Review B, 1994. **49**(20): p. 14251.
45. Kresse, G. and J. Furthmüller, *Efficiency of ab-initio total energy calculations for metals and semiconductors using a plane-wave basis set.* Computational materials science, 1996. **6**(1): p. 15-50.
46. Kresse, G. and J. Furthmüller, *Efficient iterative schemes for ab initio total-energy calculations using a plane-wave basis set.* Physical review B, 1996. **54**(16): p. 11169.
47. Blöchl, P.E., *Projector augmented-wave method.* Physical review B, 1994. **50**(24): p. 17953.
48. Kresse, G. and D. Joubert, *From ultrasoft pseudopotentials to the projector augmented-wave method.* Physical review b, 1999. **59**(3): p. 1758.
49. Perdew, J.P., K. Burke, and M. Ernzerhof, *Generalized gradient approximation made simple.* Physical review letters, 1996. **77**(18): p. 3865.
50. Dudarev, S., et al., *Electron-energy-loss spectra and the structural stability of nickel oxide: An LSDA+ U study.* Physical Review B, 1998. **57**(3): p. 1505.
51. Monkhorst, H.J. and J.D. Pack, *Special points for Brillouin-zone integrations.* Physical review B, 1976. **13**(12): p. 5188.
52. Roldán, R., et al., *Theory of 2D crystals: graphene and beyond.* Chemical Society Reviews, 2017. **46**(15): p. 4387-4399.
53. Momma, K. and F. Izumi, *VESTA 3 for three-dimensional visualization of crystal, volumetric and morphology data.* Journal of applied crystallography, 2011. **44**(6): p. 1272-1276.
54. Asbrink, S. and A. Waskowska, *CuO: X-ray single-crystal structure determination at 196 K and room temperature.* Journal of Physics: Condensed Matter, 1991. **3**(42): p. 8173.
55. Narang, S., V. Kartha, and N. Patel, *Fourier transform infrared spectra and normal vibrations of CuO.* Physica C: Superconductivity, 1992. **204**(1-2): p. 8-14.
56. Takita, Y., et al., *The promotion effect of surface hydroxyl on the oxygen adsorption over NiO, Fe2O3, and CuO.* Bulletin of the Chemical Society of Japan, 1985. **58**(6): p. 1827-1828.
57. Warren, S., et al., *Adsorption of H2O on single crystal CuO.* Surface science, 1999. **436**(1-3): p. 1-8.
58. Chen, L.-J., G.-S. Li, and L.-P. Li, *CuO nanocrystals in thermal decomposition of ammonium perchlorate.* Journal of thermal analysis and calorimetry, 2008. **91**(2): p. 581-587.
59. Sundar, S., G. Venkatachalam, and S.J. Kwon, *Biosynthesis of copper oxide (CuO) nanowires and their use for the electrochemical sensing of dopamine.* Nanomaterials, 2018. **8**(10): p. 823.
60. Almasi, H., L. Mehryar, and A. Ghadertaj, *Characterization of CuO-bacterial cellulose nanohybrids fabricated by in-situ and ex-situ impregnation methods.* Carbohydrate polymers, 2019. **222**: p. 114995.
61. Biesinger, M.C., *Advanced analysis of copper X-ray photoelectron spectra.* Surface and Interface Analysis, 2017. **49**(13): p. 1325-1334.
62. He, Y., et al., *Hydrophobic CuO nanosheets functionalized with organic adsorbates.* Journal of the American Chemical Society, 2018. **140**(5): p. 1824-1833.
63. Tauc, J., R. Grigorovici, and A. Vancu, *Optical properties and electronic structure of amorphous germanium.* physica status solidi (b), 1966. **15**(2): p. 627-637.
64. Drobny, V. and L. Pulfrey, *Properties of reactively-sputtered copper oxide thin films.* Thin solid films, 1979. **61**(1): p. 89-98.
65. Pierson, J., A. Thobor-Keck, and A. Billard, *Cuprite, paramelaconite and tenorite films deposited by reactive magnetron sputtering.* Applied surface science, 2003. **210**(3-4): p. 359-367.
66. Li, Y., et al., *CuO particles and plates: synthesis and gas-sensor application.* Materials Research Bulletin, 2008. **43**(8-9): p. 2380-2385.
67. Roth, A.P., J.B. Webb, and D.F. Williams, *Band-gap narrowing in heavily defect-doped ZnO.* Physical Review B, 1982. **25**(12): p. 7836.
68. Chaki, S., J. Tailor, and M. Deshpande, *Covellite CuS–Single crystal growth by chemical vapour transport (CVT) technique and characterization.* Materials science in semiconductor processing, 2014. **27**: p. 577-585.

Sulfur-functionalization leads to surface modification of CuO nanosheets by Cu-S structures, which imparts conductive behavior to the material